Dopant Engineering for Spiro-OMeTAD Hole-Transporting Materials towards Efficient Perovskite Solar Cells
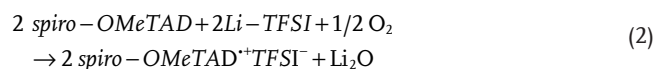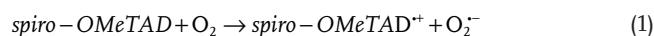
Ji-Youn Seo,* Seckin Akin, Michal Zalibera, Marco A. Ruiz Preciado, Hui-Seon Kim, Shaik M. Zakeeruddin, Jovana V. Milić,* and Michael Grätzel*

One of the most prominent hole-transporting material (HTM) for hybrid perovskite solar cells has been 2,2″,7,7″-tetrakis[*N,N*-di(4-methoxyphenyl)amino]-9,9′-spirobifluorene (spiro-OMeTAD), which is commonly doped with metal bis(trifluoromethylsulfonyl)imide (M(TFSI)$_n$) salts that contribute to generating the active radical cation HTM species. The underlying role of the metal cation, however, remains elusive. Here, the effect of metal cations (M = Li, Zn, Ca, Cu, and Sr) on doping spiro-OMeTAD is analyzed by a combination of techniques, including electron paramagnetic resonance spectroscopy and cyclic voltammetry, which is complemented by photovoltaic device and hole mobility analysis. As a result, the authors reveal the superiority of Zn(TFSI)$_2$ salts in device performances as compared to the others, including redox-active Cu(TFSI)$_2$. This analysis thereby unravels new design principles for dopant engineering in HTMs for hybrid perovskite photovoltaics.

1. Introduction

The conventional perovskite solar cell (PSC) architectures (n-i-p) are based on compact (cp) and mesoporous (mp) TiO$_2$ electron transporting material (ETM) and 2,2″,7,7″-tetrakis[*N,N*-di(4-methoxyphenyl)amino]-9,9′-spirobifluorene (spiro-OMeTAD) hole transporting material (HTM). This remains the most representative structure of the PSCs for achieving the record solar-to-electric power conversion efficiencies (PCEs).[1–10] However, low hole mobility of spiro-OMeTAD requires employing

lithium bis(trifluoromethylsulfonyl)imide (LiTFSI) as a dopant, often in conjunction with 4-(*tert*-butyl)pyridine (*t*BP) that contributes to its solubility and improves the interfacial contacts, mostly at the expense of device stability.[9,11,12] This is particularly due to the fast diffusion of lithium ions accompanied by hydrophilicity and the lowering of the glass transition temperature of spiro-OMeTAD by LiTFSI, which is assumed to play an important role in causing instability of the PSCs due to Li ion migration to the adjacent layers.[13] In addition, LiTFSI is proposed to act as a dopant in the presence of oxygen, leading to the formation of the oxidized spiro-OMeTAD based on the following Equations (1) and (2).[14–16]

$$spiro-OMeTAD + O_2 \rightarrow spiro-OMeTAD^{\cdot+} + O_2^{\cdot-} \qquad (1)$$

$$\begin{aligned} 2\ spiro-OMeTAD + 2Li-TFSI + 1/2\ O_2 \\ \rightarrow 2\ spiro-OMeTAD^{\cdot+}TFSI^- + Li_2O \end{aligned} \qquad (2)$$

However, the mode of action of HTM dopants is still not fully understood. To improve the stability and photovoltaic (PV) performance of PSCs, various dopants were studied to replace LiTFSI, such as AgTFSI,[13] Co(TFSI)$_3$ complexes,[17] and Cu(TFSI)$_2$.[18] These were nonetheless still unable to compete

J.-Y. Seo
Department of Nano Fusion Technology
Pusan National University
Busan 46241, Republic of Korea
E-mail: j-y.seo@pusan.ac.kr

J.-Y. Seo, M. A. R. Preciado, S. M. Zakeeruddin, J. V. Milić, M. Grätzel
Laboratory of Photonics and Interfaces
Institute of Chemical Sciences and Engineering
École Polytechnique Fédérale de Lausanne (EPFL)
Lausanne CH-1015, Switzerland
E-mail: jovana.milic@unifr.ch; michael.gratzel@epfl.ch

The ORCID identification number(s) for the author(s) of this article can be found under https://doi.org/10.1002/adfm.202102124.

J.-Y. Seo
Bio-IT Fusion Technology Research Institute
Pusan National University
Busan 46241, Republic of Korea

S. Akin
Department of Metallurgical and Materials Engineering
Karamanoglu Mehmetbey University
Karaman 70100, Turkey

M. Zalibera
Institute of Physical Chemistry and Chemical Physics
Faculty of Chemical and Food Technology
Slovak University of Technology
Radlinského 9, Bratislava 1 812 37, Slovakia

H.-S. Kim
Department of Chemistry
Inha University
Incheon 22212, Republic of Korea

J. V. Milić
Adolphe Merkle Institute
University of Fribourg
Fribourg 1700, Switzerland

ADVANCED
SCIENCE NEWS
www.advancedsciencenews.com

ADVANCED
FUNCTIONAL
MATERIALS
www.afm-journal.de

against the performance of LiTFSI, and they are often applied in addition to LiTFSI for achieving higher efficiency.[13,18] Alternatively, a dicationic salt of spiro-OMeTAD, spiro(TFSI)$_2$, was used to p-dope the HTM demonstrating the efficiency of around 10%,[19] which evidences the critical role of this species in the resulting charge extraction. Similarly, molybdenum tris(dithiolene)s successfully replaced LiTFSI and showed an efficiency of 16.7%, with particularly improved thermal stability.[20] We have also demonstrated Zn(TFSI)$_2$ as a potential *p*-dopant for spiro-OMeTAD that increases the hole concentration in the spiro-OMeTAD compared to LiTFSI and results in improving PV performance with higher open-circuit voltage (V_{OC}) and better photostability.[21] The discovery of effective new dopants for the spiro-OMeTAD, therefore, remains an ongoing pursuit. Towards this goal, the TFSI counterion remains the most attractive candidate due to its reduced nucleophilicity, reducing ion pairing and resulting in higher conductivity.[22,23] On the other hand, metal cations[24,25] show different p-doping effects and PV performance, and the origin of their effect remains elusive.

Herein, we investigate the oxidation of spiro-OMeTAD and doping effects by different M(TFSI)$_n$ salts (M = metal cations **Figure 1**) in solution and solid-state using a combination of techniques, including electron paramagnetic resonance (EPR) and cyclic voltammetry (CV), as well as photoluminescence (PL) spectroscopy. In addition, we analyze the PV performance and stability of the corresponding PSCs for comparison to unravel the underlying mechanism of operation that is relevant to some of the critical guiding principles of dopant engineering.

2. Results and Discussion

To analyze the effect of the dopants on PV performance, conventional mesoscopic PSCs were prepared based on triple cation (Cs, formamidinium (FA), and methylammonium (MA)) lead halide (iodide and bromide) perovskite composition as light-harvesting material.[25,27,28] In this study, M(TFSI)$_n$ salts were used as *p*-type dopants for spiro-OMeTAD at various concentration to optimize the resulting performance. While we use the PV devices for comparison, we note that the primary objective of this study is the understanding of the effect of the dopants rather than their device performances, which could be further optimized. HTM solution further employed *tert*-butylpyridine (tBP) in

chlorobenzene (CB) to enhance the miscibility of the salts in the spiro-OMeTAD matrix.[29] For this purpose, we assumed that the valency of the cation would play a role in its effectiveness to generate the spiro-OMeTAD radical cations, which is previously indicated by the superiority of Zn^{2+} as compared to Li^+ cation. In this regard, it is expected that redox-active moieties, such as Cu^{2+}, which are able to generate the active radical cation species in absence of oxygen, would be most effective. We thereby compared the performance of LiTFSI and Zn(TFSI)$_2$ to Ca(TFSI)$_2$, Cu(TFSI)$_2$, and Sc(TFSI)$_3$ as representative dopants. The details of materials, solution preparation, and device fabrication method are described in the Experimental Section. Each M(TFSI)$_n$ shows a different optimized doping ratio from the PV parameters (**Figure 2**, **Table 1**, Figure S1, Supporting Information) which are extracted from the corresponding *J*–*V* curves of PSCs (**Figure 3**a). The performances of devices with LiTFSI and Zn(TFSI)$_2$ dopants were comparable to the previous reports.[21] We thus use the optimized molar ratio of M(TFSI)$_n$ to spiro-OMeTAD, which is 0.5 for Li^+, Zn^{2+}, Ca^{2+}, Cu^{2+}, and 0.18 for Sc^{3+}, respectively. The statistical analysis of PV data shows the superiority of Zn^{2+} based on the PV parameters (Figure 2 and Table 1) as well as long-term stability (Figure 3b and Figure S6, Supporting Information). On the other hand, the results reveal that Cu^{2+} is less effective than Zn^{2+} despite its superior capacity in generating active species, which we thereby further evaluate for better understanding.

We thereafter examine the effect of M(TFSI)$_n$ on interfacial hole transfer from the perovskite to the HTM interface and the corresponding hole mobility. PL measurements were performed to compare hole transfer ability with M(TFSI)$_n$ doped HTM on the mixed halide cation perovskite film (see Experimental Section). The steady-state (**Figure 4**a) and time-resolved PL (TRPL) (Figure 4b) show faster decay lifetime with the samples of perovskite/spiro-OMeTAD doped with Zn^{2+} (26.7 ns) and Cu^{2+} (33.5 ns) as compared to Li^+ (34.9 ns), while Ca^{2+} (36.7 ns), and Sc^{2+} (40.9 ns) that show longer hole transfer times (the fitting parameters for PL decays are summarized in Table S1, Supporting Information). This suggests that Zn^{2+} and Cu^{2+} are somewhat more effective in promoting hole extraction if we assume that other factors do not contribute to the recombination process at the interface.

We assessed the capacity to generate spiro-OMeTAD radical by using electron spin resonance (ESR) spectroscopy. EPR spectra of the solutions of the species were analyzed based on the quantities of M(TFSI)$_n$ comparable to those previously investigated
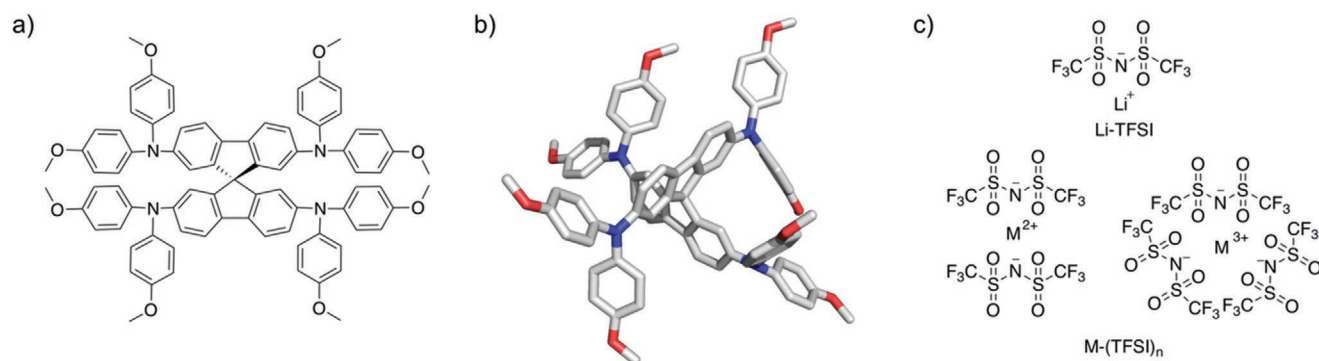
Figure 1. a) Chemical structure of spiro-OMeTAD and b) its crystal structure (CCDC no. 1475944.[26] b) Structure of LiTFSI and M(TFSI)$_n$ dopants where M = Zn^{2+}, Ca^{2+}, Cu^{2+}, and Sc^{3+}; *n* = 1, 2, 3.
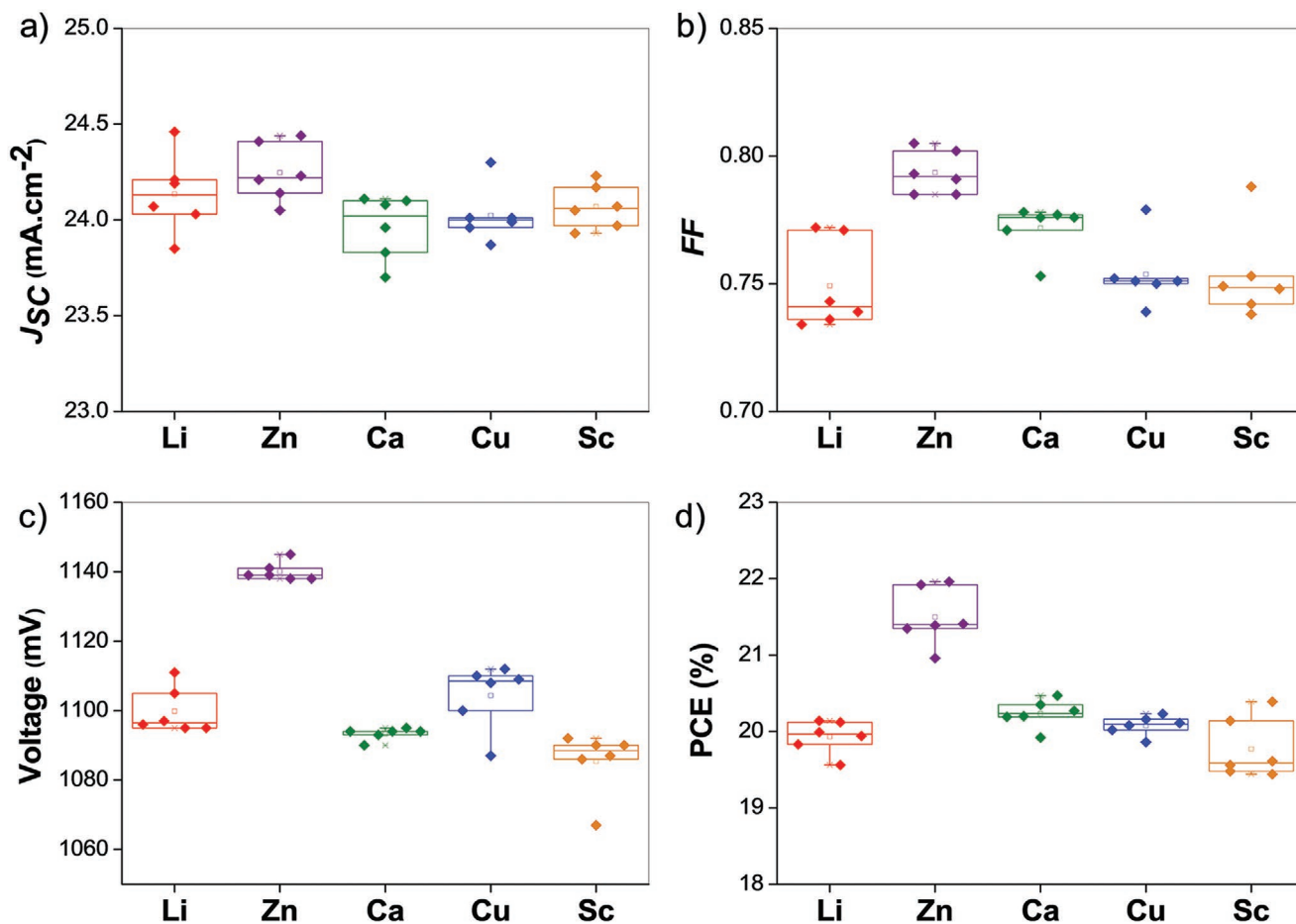
Figure 2. PV parameters collected from J–V curves of devices with $M(TFSI)_n$ (M = Li, Zn, Ca, Cu, and Sc), namely a) current density (J_{sc}), b) FF, c) open-circuit voltage (V_{oc}), and d) solar-to-electric PCE.
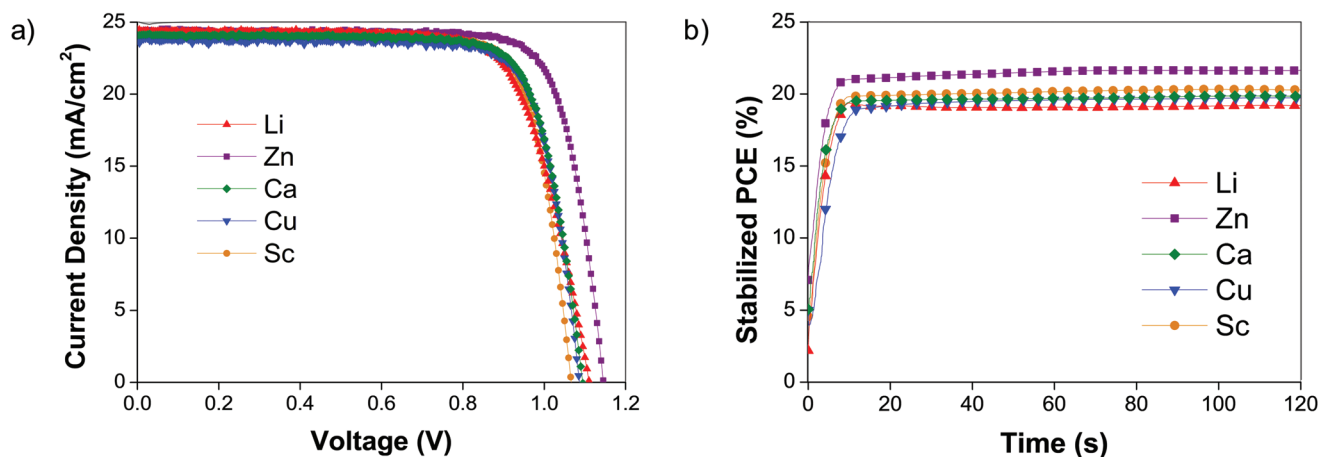
(outlined in Table S2, Supporting Information), which were monitored under identical experimental conditions (**Figure 5**a and Figure S2a, Supporting Information). A singlet EPR signal with $g_{iso} = 2.0033 \pm 0.0002$ typical for the organic cation radical of spiro-OMeTAD was observed with all dopants, evidencing that the oxidation of spiro-OMeTAD occurs even under anaerobic conditions and it is enhanced when the solutions are measured under illumination.[16] In the case of $Cu(TFSI)_2$, this signal was accompanied by the signals from the paramagnetic Cu^{2+} complexes, which were subtracted from the spectra for the quantitative evaluation of the spiro-OMeTAD cations formed. The reaction in the dark proceeds with different kinetics for each

complex. However, at the given 1/10 dopant/spiro-OMeTAD molar ratio, negligible concentrations of the radical cation form for LiTFSI and $Zn(TFSI)_2$ dopants as well as $Ca(TFSI)_2$ and $Sc(TFSI)_3$. On the contrary, a significantly stronger EPR signal was observed for samples doped with $Cu(TFSI)_2$, indicating a different mechanism of radical cation radical formation, likely through a direct redox reaction.[18] Irradiation with visible light leads to the increase of the spiro-OMeTAD radical cation signal with a different kinetic profile for each dopant (Figure 5b,c, and Figure S2b, Supporting Information). After almost 3 h of irradiation, the concentration of spiro-OMeTAD cations reached a comparable concentration for $Zn(TFSI)_2$ and $Cu(TFSI)_2$ of about 80–85 µM whereas only about 10 µM with LiTFSI, two orders of magnitude lower than the dopant concentration.

The difference in the concentration of the radical cation with different dopants can be also observed from the color of the solution (reddish-brown) and could be followed spectrophotometrically. We have thus also monitored the UV/Vis/NIR absorption spectra of spiro-OMeTAD/tBP solutions with the most effective $Zn(TFSI)_2$ dopants and compared it to LiTFSI in the nitrogen-filled glovebox. Continuous irradiation with a low-intensity lamp of the spectrometer induces the solution coloring, which is assigned to the formation of the spiro-OMeTAD radical cations.[17,20,30,31] The species features a visible

Table 1. PV parameters of champion devices with optimized $M(TFSI)_n$ doping.

M	J_{sc}/mA cm^{-2}	V_{oc}/V	FF	PCE/%
Li	24.16	1.11	0.73	20.1
Zn	24.40	1.15	0.79	22.0
Ca	24.10	1.10	0.78	20.5
Cu	23.86	1.09	0.78	20.2
Sc	24.23	1.07	0.79	20.4

**ADVANCED
SCIENCE NEWS**
www.advancedsciencenews.com

**ADVANCED
FUNCTIONAL
MATERIALS**
www.afm-journal.de

Figure 3. PV performance of PSCs. a) Current density–voltage (*J–V*) curves and b) stabilized PCE at maximum power point (mpp) of the devices employing M(TFSI)$_n$ as a dopant for spiro-OMeTAD. The *J–V* curves are taken at 10 mV s^{-1} scan rate under AM1.5G simulated solar light. The device active area is defined using a black metal shadow mask with an aperture area of 0.16 cm^2.

absorption band with around 530 nm and an intense near-infrared band with a maximum of around 1600 nm (Figure S3, Supporting Information). This suggests that the efficiency of the cation formation is higher with the Zn(TFSI)$_2$ dopant, in accordance with the EPR results.

CV measurements were therefore conducted to understand the unexpected behavior of Cu(TFSI)$_2$ as compared to Zn(TFSI)$_2$ on device performance and further clarify the oxidation mechanism of spiro-OMeTAD. The redox properties of the Li(TFSI), Zn(TFSI)$_2$, Ca(TFSI)$_2$, Cu(TFSI)$_2$, and Sc(TFSI)$_3$, as well as spiro-OMeTAD, were probed by CV in CH$_3$CN (Figure S4, Supporting Information). While Li(TFSI), Ca(TFSI)$_2$, and Sc(TFSI)$_3$ are redox-inactive in a large potential range, showing only irreversible reduction at negative potentials beyond −2.5 V versus Fc$^+$/Fc, in accordance with reports in the literature and their applications as supporting electrolytes,[32] Zn(TFSI)$_2$ shows an irreversible reduction at −1.5 V. In the CV back-scan, a trace crossing was observed with an intense adsorption re-oxidation peak occurred at −0.85 V.

Such voltammetric response can be likely explained by a two-electron reduction of Zn^{2+} followed by the adsorption of metallic Zn^0 at the electrode and its re-oxidation to Zn^{2+} and dissolution during the back scan. In contrast, Cu(TFSI)$_2$ shows a reversible redox process at 0.64 V versus Fc$^+$/Fc and an irreversible reduction at E_p of −0.88 V. In the CV back-scan, several adsorption re-oxidation peaks in the −0.15 to −0.75 V potential range can be likely linked with the reverse of this process. The Cu^{2+}/Cu$^+$ reduction can be assigned to a redox couple at 0.64 V and a reduction of Cu$^+$/Cu^0 to the irreversible event at −0.88 V. The latter would be followed by uptake of solid particles by spiro-OMeTAD, which otherwise shows two reversible successive single-electron oxidations at 0.13 and 0.33 V versus Fc$^+$/Fc, and an additional irreversible two-electron oxidation at peak potential E_p of 0.99 V. A quasi-reversible reduction at rather negative −3 V was also detected. These results are in line with a previous study where only reversible redox events were observed.[33] The comparison of the Cu^{2+}/Cu$^+$ reduction potential of Cu(TFSI)$_2$ (0.64 V versus Fc$^+$/Fc) with the oxidation
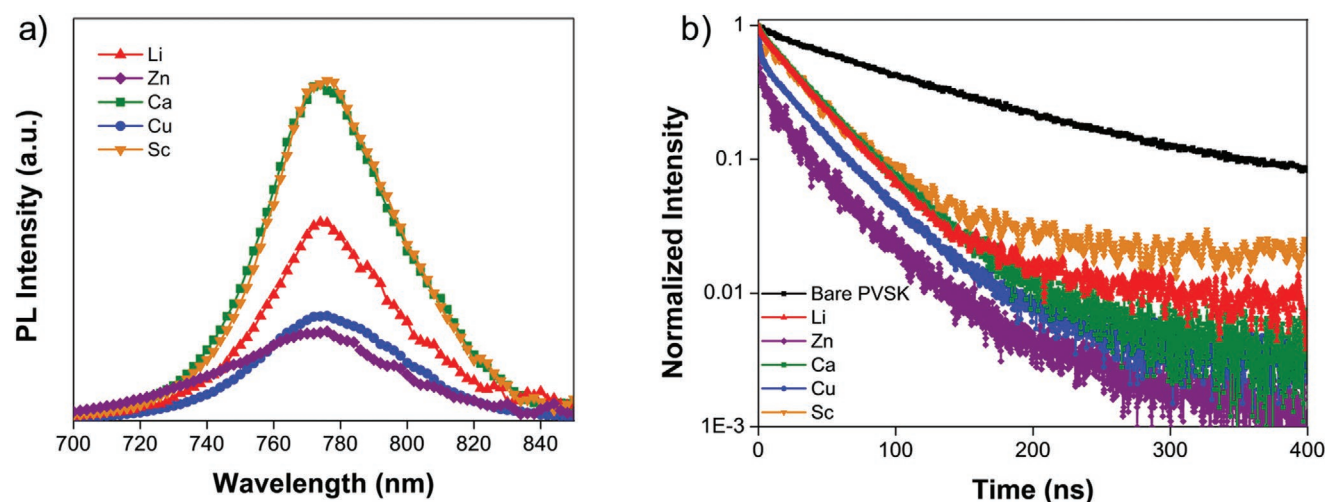
Figure 4. a) Steady-state PL emission spectra and b) normalized TRPL decay plots of the spiro-OMeTAD films with various M(TFSI)$_n$ dopants (M = Li$^+$, Zn^{2+}, Ca^{2+}, Cu^{2+}, and Sc^{3+}).
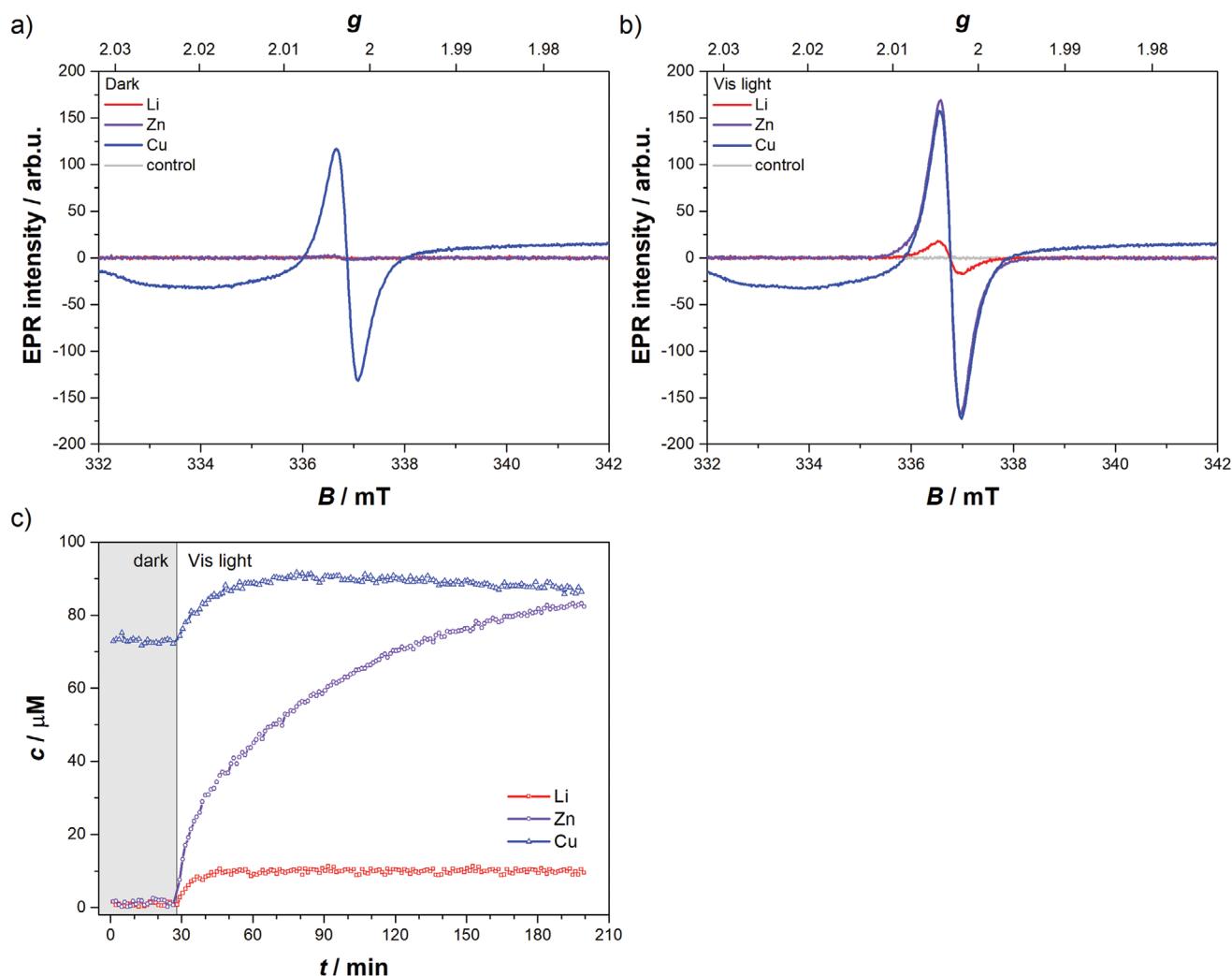
Figure 5. a) The continuous-wave EPR spectroscopy (CW-EPR) spectra (X-band, 296 K) of the spiro-OMeTAD/tBP CB solutions with the LiTFSI, Zn(TFSI)$_2$, and Cu(TFSI)$_2$ dopants after 25 min of measurements without illumination under oxygen-free conditions. b) The EPR spectra after 170 min of irradiation with Vis light (200 min total exp. time). EPR spectra with other dopants are shown in Figure S2, Supporting Information. c) The spiro-OMeTAD cation radical concentration dependence on the irradiation time.

potentials of Spiro-OMeTAD (0.13 and 0.33 V versus Fc$^+$/Fc) shows that the Cu(TFSI)$_2$ has sufficient oxidative power to directly oxidize Spiro-OMeTAD to the radical cation. Alternatively, two Cu(TFSI)$_2$ molecules can oxidize Spiro-OMeTAD even to the dication, and the formation of higher oxidized states were indeed previously detected upon the reaction of Cu(TFSI)$_2$ with Spiro-OMeTAD in CB.[18] However, the HTM solutions and films studied in this work were prepared with an excess of tBP. Pyridine and its derivatives belong to the most prominent coordinating ligands in organometallic chemistry and the formation of Cu(tBP)$_n^{2+}$ (n = 4–6) is thus a likely scenario. The coordination of tBP was confirmed by EPR in frozen solutions at 77 K (Figure S5b, Supporting Information). The spectrum of Cu(TFSI)$_2$ in CB undergoes significant changes upon addition of tBP, including the decrease of the principal g-tensor values and the increase of the Cu hyperfine couplings. Moreover, the super-hyperfine structure due to interaction with coordinated tBP nitrogens was observed

in the spectrum. Unfortunately, the spectral resolution was insufficient for unambiguous determination of the number of coordinated tBPs, but, in line with previous studies,[34] we estimate it to exceed 4 (n > 4, the best-fit simulation of the Cu(tBP)$_n^{2+}$ EPR record in Figure S5b, Supporting Information, was obtained with n = 6). The coordination of tBP also has a significant impact on the redox properties of the Cu^{2+}/Cu$^+$ couple. The CV of Cu(TFSI)$_2$ with 8 equivalents of tBP shows an electrochemically irreversible Cu^{2+} reduction with E_p of –0.43 V versus Fc$^+$/Fc accompanied by a shifted re-oxidation peak at E_p of 0.60 V in the back scan (Figure S5a, Supporting Information). The irreversibility is likely caused by reconstitution of the coordination sphere in Cu(tBP)$_n^{2+/+}$ between the Cu^{2+} and Cu$^+$ oxidation states. More importantly, the significant drop of the Cu^{2+} reduction potential upon coordination of tBP makes it essentially ineffective in the oxidation of spiro-OMeTAD. The amount of spiro-OMeTAD$^{·+}$ formed upon the addition of Cu(TFSI)$_2$ to the solutions of spiro-OMeTAD/tBP

will thus depend on the kinetic balance between the direct oxidation and Cu^{2+} coordination with tBP, explaining thus the relatively low radical cation yields reported above. The coordination of tBP ligands plays also an essential role within the recently proposed mechanism for the spiro-OMeTAD oxidation by $Zn(TFSI)_2$ in oxygen-free dark environment.[35] As a result, while the redox activity of $Cu(TFSI)_2$ is expected to facilitate the formation of active spiro-OMeTAD radical cations, the coordination with tBP renders the resulting process less effective than the one mediated by $Zn(TFSI)_2$, which provides critical insights about the underlying process that is relevant in the PSC operation.

3. Conclusion

In summary, this study reveals the importance of an interplay of valency, ion size, and redox activity of the $M(TFSI)_n$ dopants (M = Li^+, Zn^{2+}, Cu^{2+}, Ca^{2+}, and Sc^{3+}) in their capacity to increase the hole mobility of HTMs, spiro-OMeTAD in particular, without compromising the stability of the resulting PV devices. In this regard, redox-active dopants, such as $Cu(TFSI)_2$, are found not to be necessarily superior despite their capacity to effectively generate active spiro-OMeTAD radical cation species. Moreover, this assessment confirms that $Zn(TFSI)_2$ provides an optimal trade-off between the radical cation generation and the resulting hole mobility and it could thereby serve as an appropriate replacement for more commonly used $Li(TFSI)$. As a result, photo-generated electrons are extracted rapidly producing a very high fill factor (FF) of close to 80% a V_{OC} of 1.15 V and a PCE > 21.9%, setting a stage for further advancing PSC devices.

4. Experimental Section

Substrate and mp-TiO_2 Preparation: Nippon Sheet Glass 10 Ω sq^{-1} was cleaned by sonication in 2% Hellmanex water solution for 30 min. After rinsing with deionized water and ethanol, the substrates were further cleaned with UV ozone treatment for 15 min. Then, ≈30 nm TiO_2 compact layer was deposited on FTO via spray pyrolysis at 450 °C from a precursor solution of titanium diisopropoxide bis(acetylacetonate) in anhydrous ethanol (1:9, volume ratio). After the spraying, the substrates were kept at 450 °C for 45 min and left to cool down to room temperature. TiO_2 paste (30 NR-D, Dyesol) diluted in ethanol (1:6, weight ratio) was used for mp-TiO_2 layer. The mp-TiO_2 layer was deposited by spin coating for 20 s at 4000 rpm with a ramp of 2000 rpm per s to achieve a 150–200 nm thick layer. After the spin coating, the substrates were immediately dried at 100 °C for 10 min and then sintered again at 450 °C for 30 min under dry air flow. After cooling down to 150 °C the substrates were immediately transferred into a nitrogen atmosphere glove box for depositing the perovskite films.

Perovskite Precursor Solution and Film Preparation: The organic cations were purchased from Dyesol; the lead compounds from TCI; CsI from abcr GmbH. The perovskite precursors were dissolved in anhydrous DMF:DMSO (4:1, v:v). It was noted that 10% excess PbI_2 and $PbBr_2$ were used for perovskite precursor solution The perovskite precursor solution was prepared by dissolving a mixture of FAI (1.0 M), PbI_2 (1.1 M), MABr (0.2 M), and $PbBr_2$ (0.2 M) in 1 mL of a mixed solution of DMF and DMSO under the mild heating condition at ≈70 °C to assist dissolving. Then CsI, pre-dissolved as a 1.5 M stock solution in DMSO, was added to the mixed perovskite (FA/MA) precursor to make Cs/FA/MA triple cation perovskite. The perovskite solution was spin-coated in a two steps program at 1000 and 4000 rpm for 10 and 20 s, respectively. During the

second step, 200 µL of CB was poured on the spinning substrate 15 s before the end of the program. The substrates were then annealed at 100 °C for 45 min in a nitrogen-filled glove box.

HTM Solution and Films Preparation: After the perovskite annealing, the substrates were cooled down for few minutes and a spiro-OMeTAD (Merck) solution (70 mM in CB) was spin-coated at 4000 rpm for 20 s. Spiro-OMeTAD was doped with M-$(TFSI)_n$ and 4-*tert*-Butylpyridine (tBP, Sigma-Aldrich). The molar ratio of additives for spiro-OMeTAD is listed in Supporting Information. Finally, 70–80 nm of the gold top electrode was thermally evaporated under high vacuum.

PV Device Measurements: The solar cells were measured using a 450 W xenon light source (Oriel). The spectral mismatch between AM1.5G and the simulated illumination was reduced by the use of a Schott K113 Tempax filter (Präzisions Glas & Optik GmbH). The light intensity was calibrated with a Si photodiode equipped with an IR-cutoff filter (KG3, Schott), and it was recorded during each measurement. Current–voltage characteristics of the cells were obtained by applying an external voltage bias while measuring the current response with a digital source meter (Keithley 2400). The voltage scan rate was 10 mV s^{-1} and no device preconditioning, such as light soaking or forward voltage bias, was applied before starting the measurement. The starting voltage was determined as the potential at which the cells furnish 1 mA in forward bias, no equilibration time was used. The cells were masked with a black metal mask (0.16 cm^2) to fix the active area and reduce the influence of the scattered light. The long-term stability tests of unencapsulated devices were monitored by storing the devices under dark at a relative humidity of 50 ± 5%. The PV performance of the devices was periodically measured under the AM 1.5G simulated solar light.

EPR measurements were performed with the X-band EMX-plus spectrometer (Bruker, Germany) at 296 K ambient temperature. The (2,2,6,6-Tetramethylpiperidin-1-yl)oxyl (TEMPO) nitroxide radical solution in CB served as a calibration standard for quantification. All solvents and liquid reagents were purged with Ar for 30 min before insertion to GB where they were stored under N_2 atmosphere. The solutions were prepared by mixing 500 µL of the stock solution containing Spiro-OMeTAD/tBP/CB with 17.5 µL of 0.2 M M$(TFSI)_n$ metal complex CH_3CN solutions to achieve final concentrations listed in Table S2, Supporting Information. 100 µL of these mixtures were filled into the 3 mm NMR tubes, sealed by a stopper, and wrapped with parafilm tape for EPR experiments and the rest of the solution was poured into a UV/Vis cuvette and analyzed under inter atmosphere in the glovebox. The samples were irradiated with the unfiltered light of a Vis Schott KL 1600 LED (650 lm luminous lux). In the initial trial series samples containing all investigated dopants were irradiated ex situ for 60 min. In the second set of experiments, the selected samples were further investigated during a 3 h in situ irradiation in the cavity of the HQ resonator. The mixtures with $Cu(TFSI)_2$ as well as control samples w/o tBP, and/or w/o spiro-OMeTAD were additionally investigated at 77 K.

The UV/Vis/NIR absorption spectra of the spiro-OMeTAD/tBP solution were recorded by a spectrophotometer (Lambda 1050+, Perkin Elmer). The steady-state PL measurement was performed using a fluorescence spectrometer (FLS920P, Edinburgh Instruments) by exciting the samples at a fixed wavelength of 460 nm and scanning the emission monochromator from 700 to 850 nm. The TRPL decay transients were measured using a picosecond pulsed diode laser (EPL-405; Edinburgh Instruments) as the single wavelength excitation light source.

CV experiments were performed with solutions of LiTFSI, $Zn(TFSI)_2$, $Ca(TFSI)_2$, $Cu(TFSI)_2$, $Sc(TFSI)_3$, or Spiro-OMeTAD in 0.1 M tetrabutylammonium hexafluorophosphate (nBu_4NPF_6) supporting electrolyte in CH_3CN were performed under argon atmosphere using a three-electrode arrangement with glassy carbon 1 mm disc working electrode (from Ionode, Australia), a platinum wire as the counter electrode, and silver wire as the pseudo- reference electrode. Sample concentration was in the low mM range (few crystals dissolved in 1 mL of electrolyte solution). Ferrocene (Fc) served as the internal potential standard. A Heka PG310USB (Lambrecht, Germany) potentiostat with a PotMaster 2.73 software package served for the potential control in voltammetry studies.

Supporting Information

Acknowledgements

Conflict of Interest

The authors declare no conflict of interest.

Data Availability Statement

Research data are not shared.

Keywords

[1] H. S. Kim, C. R. Lee, J. H. Im, K. B. Lee, T. Moehl, A. Marchioro, S. J. Moon, R. Humphry-Baker, J. H. Yum, J. E. Moser, M. Gratzel, N. G. Park, *Sci. Rep.* **2012**, *2*, 591.

[2] M. M. Lee, J. Teuscher, T. Miyasaka, T. N. Murakami, H. J. Snaith, *Science* **2012**, *338*, 643.

[3] G. Giorgi, J. I. Fujisawa, H. Segawa, K. Yamashita, *J. Phys. Chem. Lett.* **2013**, *4*, 4213.

[4] G. C. Xing, N. Mathews, S. Y. Sun, S. S. Lim, Y. M. Lam, M. Gratzel, S. Mhaisalkar, T. C. Sum, *Science* **2013**, *342*, 344.

[5] S. D. Stranks, G. E. Eperon, G. Grancini, C. Menelaou, M. J. P. Alcocer, T. Leijtens, L. M. Herz, A. Petrozza, H. J. Snaith, *Science* **2013**, *342*, 341.

[6] H. M. Zhu, K. Miyata, Y. P. Fu, J. Wang, P. P. Joshi, D. Niesner, K. W. Williams, S. Jin, X. Y. Zhu, *Science* **2016**, *353*, 1409.

[7] K. Miyata, T. L. Atallah, X. Y. Zhu, *Sci. Adv.* **2017**, *3*, e1701469.

[8] K. X. Steirer, P. Schulz, G. Teeter, V. Stevanovic, M. Yang, K. Zhu, J. J. Berry, *ACS Energy Lett.* **2016**, *1*, 360.

[9] X. Zhao, H. S. Kim, J. Y. Seo, N. G. Park, *ACS Appl. Mater. Interfaces* **2017**, *9*, 7148.

[10] NREL, http://www.nrel.gov/pv/assets/images/efficiency-chart.png (accessed: March 2021).

[11] H. S. Kim, J. Y. Seo, N. G. Park, *J. Phys. Chem. C* **2016**, *120*, 27840.

[12] H. S. Kim, J. Y. Seo, N. G. Park, *ChemSusChem* **2016**, *9*, 2528.

[13] B. Xu, J. Huang, H. Agren, L. Kloo, A. Hagfeldt, L. C. Sun, *ChemSusChem* **2014**, *7*, 3252.

[14] K. Domanski, E. A. Alharbi, A. Hagfeldt, M. Gratzel, W. Tress, *Nat. Energy* **2018**, *3*, 61.

[15] A. Abate, T. Leijtens, S. Pathak, J. Teuscher, R. Avolio, M. E. Errico, J. Kirkpatrik, J. M. Ball, P. Docampo, I. McPherson, H. J. Snaith, *Phys. Chem. Chem. Phys.* **2013**, *15*, 2572.

[16] M. Namatame, M. Yabusaki, T. Watanabe, Y. Ogomi, S. Hayase, K. Marumoto, *Appl. Phys. Lett.* **2017**, *110*, 123904.

[17] J. Burschka, F. Kessler, M. K. Nazeeruddin, M. Gratzel, *Chem. Mater.* **2013**, *25*, 2986.

[18] J. Mohanraj, M. Stihl, E. Simon, O. von Sicard, G. Schmid, M. Fleischer, C. Neuber, M. Thelakkat, *ACS Appl. Energy Mater.* **2019**, *2*, 3469.

[19] W. H. Nguyen, C. D. Bailie, E. L. Unger, M. D. McGehee, *J. Am. Chem. Soc.* **2014**, *136*, 10996.

[20] A. Pellaroque, N. K. Noel, S. N. Habisreutinger, Y. D. Zhang, S. Barlow, S. R. Marder, H. J. Snaith, *ACS Energy Lett.* **2017**, *2*, 2044.

[21] J. Y. Seo, H. S. Kim, S. Akin, M. Stojanovic, E. Simon, M. Fleischer, A. Hagfeldt, S. M. Zakeeruddin, M. Gratzel, *Energy Environ. Sci.* **2018**, *11*, 2985.

[22] H. Djellab, M. Armand, D. Delabouglise, *Synth. Met.* **1995**, *74*, 223.

[23] M. Armand, F. Endres, D. R. MacFarlane, H. Ohno, B. Scrosati, *Nat. Mater.* **2009**, *8*, 621.

[24] S. Akin, N. Arora, S. M. Zakeeruddin, M. Gratzel, R. H. Friend, M. I. Dar, *Adv. Energy Mater.* **2020**, *10*, 1903090.

[25] J. T. W. Wang, Z. P. Wang, S. Pathak, W. Zhang, D. W. deQuilettes, F. Wisnivesky-Rocca-Rivarola, J. Huang, P. K. Nayak, J. B. Patel, H. A. M. Yusof, Y. Vaynzof, R. Zhu, I. Ramirez, J. Zhang, C. Ducati, C. Grovenor, M. B. Johnston, D. S. Ginger, R. J. Nicholas, H. J. Snaith, *Energy Environ. Sci.* **2016**, *9*, 2892.

[26] D. Shi, X. Qin, Y. Li, Y. He, C. Zhong, J. Pan, H. L. Dong, W. Xu, T. Li, W. P. Hu, J. L. Bredas, O. M. Bakr, *Sci. Adv.* **2016**, *2*.

[27] M. Saliba, T. Matsui, J. Y. Seo, K. Domanski, J. P. Correa-Baena, M. K. Nazeeruddin, S. M. Zakeeruddin, W. Tress, A. Abate, A. Hagfeldt, M. Gratzel, *Energy Environ. Sci.* **2016**, *9*, 1989.

[28] F. Zheng, W. J. Chen, T. L. Bu, K. P. Ghiggino, F. Z. Huang, Y. B. Cheng, P. Tapping, T. W. Kee, B. H. Jia, X. M. Wen, *Adv. Energy Mater.* **2019**, *9*, 1901016.

[29] B. Xu, Z. L. Zhu, J. B. Zhang, H. B. Liu, C. C. Chueh, X. S. Li, A. K. Y. Jen, *Adv. Energy Mater.* **2017**, *7*, 1700683.

[30] C. Chen, W. Zhang, J. Y. Cong, M. Cheng, B. B. Zhang, H. Chen, P. Liu, R. F. Li, M. Safdari, L. Kloo, L. C. Sun, *ACS Energy Lett.* **2017**, *2*, 497.

[31] S. Fantacci, F. De Angelis, M. K. Nazeeruddin, M. Gratzel, *J. Phys. Chem. C* **2011**, *115*, 23126.

[32] G. H. Lane, E. Jezek, *Electrochim. Acta* **2014**, *150*, 173.

[33] K. Zhang, L. Wang, Y. L. Liang, S. Q. Yang, J. Liang, F. Y. Cheng, J. Chen, *Synth. Met.* **2012**, *162*, 490.

[34] W. L. Hoffeditz, M. J. Katz, P. Deria, G. E. Cutsail, M. J. Pellin, O. K. Farha, J. T. Hupp, *J. Phys. Chem. C* **2016**, *120*, 3731.

[35] Y. Saygili, H. S. Kim, B. W. Yang, J. J. Suo, A. B. Munoz-Garcia, M. Pavone, A. Hagfeldt, *ACS Energy Lett.* **2020**, *5*, 1271.